

Understanding Charge Collection Mechanisms in InGaAs FinFETs Using High-Speed Pulsed-Laser Transient Testing With Tunable Wavelength

Kai Ni, *Student Member, IEEE*, Andrew L. Sternberg, *Member, IEEE*, En Xia Zhang, *Senior Member, IEEE*, John A. Kozub, Rong Jiang, *Student Member, IEEE*, Ronald D. Schrimpf, *Fellow, IEEE*, Robert A. Reed, *Fellow, IEEE*, Daniel M. Fleetwood, *Fellow, IEEE*, Michael L. Alles, *Member, IEEE*, Dale McMorrow, *Senior Member, IEEE*, Jianqiang Lin, *Student Member, IEEE*, Alon Vardi, *Student Member, IEEE*, and Jesús del Alamo, *Fellow, IEEE*

Abstract—A tunable wavelength laser system and high-resolution transient capture system are introduced to characterize transients in high-mobility MOSFETs. The experimental configuration enables resolution of fast transient signals and new understanding of charge collection mechanisms. The channel layer is critical in the charge collection process for the InGaAs FinFETs examined here. The transient current mainly comes from the channel current, due to shunt effects and parasitic bipolar effects, instead of the junction collection. The charge amplification factor is found to be as high as 14, which makes this technology relatively sensitive to transient radiation. The peak current is inversely proportional to the device gate length. Simulations show that the parasitic bipolar effect is due to source-to-channel barrier lowering caused by hole accumulation in the source and channel. Charge deposited in the channel causes prompt current, while charge deposited below the channel causes delayed and slow current.

Index Terms—III-V, charge collection, InGaAs, MOSFETs, single-event transient, technology computer-aided design (TCAD), two-photon absorption (TPA).

I. INTRODUCTION

III-V MATERIALS, especially InGaAs, have been considered to be promising channel materials for sub-10-nm nMOSFETs, due to their high electron mobility and injection velocity [1]. Moreover, for good electrostatics in

sub-10-nm technologies, multigate transistor architectures with InGaAs channels have been demonstrated [2], [3]. In space applications, the devices will be exposed to ionizing particles. In this paper, the radiation response and charge collection mechanisms of InGaAs FinFETs are investigated.

Charge collection mechanisms have been investigated in III-V FETs with noninsulating gate dielectrics, including MESFETs and HEMTs [4], and planar III-V MOSFETs with different architectures, including quantum-well InGaAs MOSFETs [5] and surface-channel GaAs MOSFETs [6]. Significant charge enhancement may occur in these devices due to parasitic bipolar effects. On the other hand, FinFET-based CMOS technologies are reported to have lower soft error rates (SER) compared with planar technologies, and further FinFET scaling reduces the SER [7], [8]. This is because of the smaller geometrical footprint of FinFET devices compared with corresponding planar devices [9]. Therefore, the two competing mechanisms (charge enhancement versus reduced size) make it interesting to study the single-event effect (SEE) sensitivity of InGaAs FinFETs.

Pulsed-laser testing has become a valuable method to study SEE in devices and circuits [10], [11]. Although the charge generation mechanisms and charge profile induced by laser irradiation are different from heavy ion irradiation, laser testing provides a complementary, nondestructive, convenient, and low-cost method for identifying the mechanisms responsible for SEE. Pulsed-laser testing can be divided into two categories: single-photon absorption (SPA) and two-photon absorption (TPA), depending on the electron-hole pair generation mechanism [12].

SPA refers to above band gap optical excitation, for which each absorbed photon generates a single electron-hole pair. Due to the exponential attenuation of the light intensity as it propagates through the material, the penetration depth of the optical pulse can be limited. To generate charge tracks with various depths, the laser wavelength is varied [13]. For SPA irradiation, however, it is often difficult or impossible to

Manuscript received February 19, 2017; revised April 22, 2017; accepted April 25, 2017. Date of publication April 28, 2017; date of current version August 15, 2017. This work was supported by the Defense Threat Reduction Agency through its fundamental research program.

K. Ni, A. L. Sternberg, E. X. Zhang, R. Jiang, R. D. Schrimpf, R. A. Reed, D. M. Fleetwood, and M. L. Alles are with the Department of Electrical Engineering and Computer Science, Vanderbilt University, Nashville, TN 37235 USA (e-mail: jnkxb.work@gmail.com).

J. A. Kozub is with the Department of Physics, Vanderbilt University, Nashville, TN 37235 USA.

D. McMorrow is with the Naval Research Laboratory, Washington, DC 20375 USA.

J. Lin, A. Vardi, and J. del Alamo are with the Microsystems Technology Laboratories, Massachusetts Institute of Technology, Cambridge, MA 02139 USA.

Color versions of one or more of the figures in this paper are available online at <http://ieeexplore.ieee.org>.

Digital Object Identifier 10.1109/TNS.2017.2699482

inject charge into a device, due to the presence of metal over layers. This challenge is addressed by utilizing TPA, which is produced by irradiation with high peak power, femtosecond laser pulses at subband gap wavelengths. Electron-hole pairs are only generated in the focal region of the laser beam, where the optical field intensity is high enough to stimulate the absorption of two photons simultaneously. This enables backside irradiation, thus addressing the problem of metal over layers [14].

Typically, TPA laser wavelengths of 1250 to 1300 nm are used for conventional silicon CMOS, for which the photon energy is below the Si bandgap. However, with CMOS scaling continuing to sub-10-nm nodes, high mobility channel materials, such as InGaAs and Ge, are likely to be introduced [1], [15]. The integration of these new materials will also necessitate incorporation of other materials, creating a complex multilayer structure with multiple bandgaps. Therefore, a single laser wavelength tuned for Si may not be sufficient for characterizing SEE in these new materials. Charge generation at a wavelength of 1260 nm will lead to mixed SPA and TPA in different layers, depending on material band gaps, such as shown in [5], [16], and [17]. In studying the charge-collection mechanisms in these multilayer structure devices, it is both necessary and difficult to identify the roles of different layers. Thus, a laser with tunable wavelength is helpful for injecting charge primarily into a specific layer, e.g., the channel.

Time-resolved SEE measurements are usually conducted with digital sampling oscilloscopes [18]. For fast transients, or fast edge characterization, it is desirable to have enough time resolution to resolve signals on the same timescale as the device response. The highest bandwidth oscilloscope reported is a 70 GHz superconducting sampling oscilloscope, which has sub-10-ps resolution [19]. However, this oscilloscope needs additional cooling and can only capture limited time window transients, so it is not practical for most testing. Almost all the other transient capture experiments that have been reported are conducted with oscilloscopes with bandwidths less than or approximately equal to 20 GHz [5], [16], [17], [20]. These have limited capability to resolve fast transient signals.

In this paper, we describe a tunable wavelength laser system that can inject charge into a specific layer in the device and capture transients with a 36-GHz bandwidth oscilloscope. We show that these new capabilities lead to enhanced insight into charge collection mechanisms in advanced devices.

II. DEVICE DESCRIPTIONS

The device under test is a double-gate InGaAs FinFET. The cross-sectional and side-view schematic of the device are shown in Fig. 1(a) and (b), respectively. The detailed fabrication process is described in [21]. A 0.4- μm -thick $\text{In}_{0.52}\text{Al}_{0.48}\text{As}$ buffer layer is grown on a 600- μm -thick semi-insulating InP substrate. A 40-nm-thick $\text{In}_{0.53}\text{Ga}_{0.47}\text{As}$ channel is grown on top of the buffer layer. The fin height is 220 nm. On top of the fin, there is a SiO_2 hard mask about 40 nm thick. A 5-nm Al_2O_3 gate dielectric is deposited by

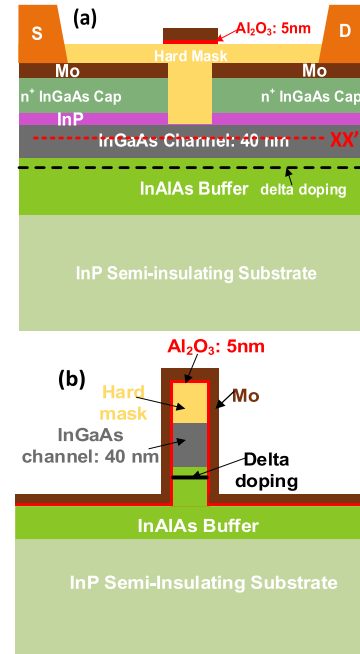


Fig. 1. (a) Cross-sectional and (b) side-view schematic of InGaAs double-gate FinFETs.

atomic layer deposition. The thick hard mask electrostatically decouples the top gate from the channel. As a result, this device is only controlled by the two side gates.

Along the fin width direction, the InGaAs channel and Al_2O_3 gate dielectric form a deep type I quantum-well. Along the fin height direction, the InGaAs channel, InAlAs buffer and SiO_2 also form a type I quantum-well, similar to planar InGaAs quantum-well MOSFETs [5]. Thus, carriers are effectively confined in the channel layer, making the channel layer critical to the charge collection process. This is an intermediate case between a bulk device and a silicon on insulator (SOI) device, in the sense that carriers are confined in the channel, but the back barrier is not high enough to fully isolate the channel from the substrate.

In this paper, devices with different gate lengths and fin widths are studied with a pulsed laser at different wavelengths. There are 11 parallel fins in each tested device. The fin spacing is 0.8 μm . For transient capture, all the devices are mounted in custom-milled metal packages with microstrip transmission lines and precision 2.92-mm K connectors [5], [16].

To compare an older limited bandwidth transient capture system with the new higher bandwidth system, transients of planar InGaAs quantum-well MOSFETs, captured by the two systems are given. More device details are described in [5] and [22]. The charge collection mechanisms have been discussed in [5]; in this paper, the charge collection results obtained in the planar InGaAs quantum-well MOSFETs are included only for system-comparison purposes.

III. EXPERIMENTAL SETUP

Pulsed-laser testing experiments were performed at Vanderbilt University. The laser system setup is shown schematically in Fig. 2 [23]. It utilizes a titanium-sapphire (Ti/S) pumped optical parametric generator (OPG).

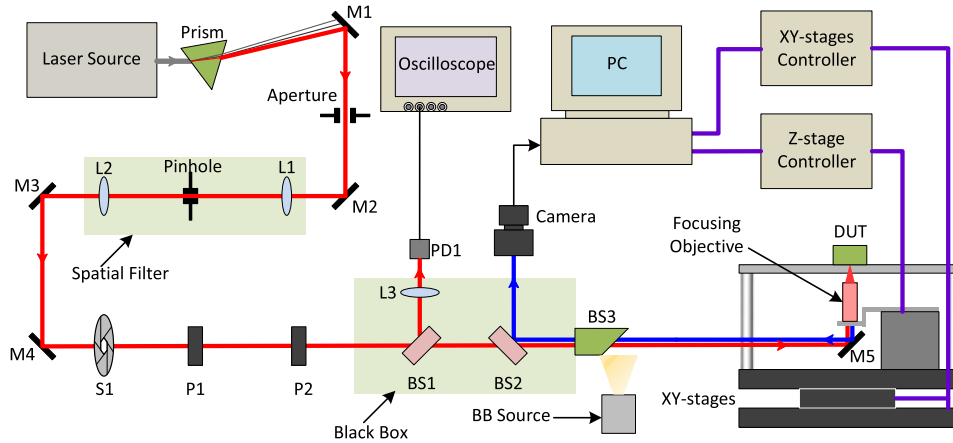


Fig. 2. Simplified block diagram of TPA test setup. In the figure, “L” stands for lens, “M” stands for mirror, “S” stands for shutter, “P” stands for polarizer, “BS” stands for beam splitter, “PD” stands for photodiode, and “BB” represents the broadband light source. The red line indicates the optical path traveled by the laser beam. The blue line indicates the reflected light that is imaged by the near IR camera.

The OPG is pumped at a 1 kHz repetition rate with 1 mJ, 150 fs pulses centered at 800 nm from a chirped-pulse amplifier. The amplifier is seeded with a passively mode-locked Ti/S oscillator. The OPG uses nonlinear parametric frequency conversion in a beta barium borate crystal to generate and amplify signal and idler wavelengths that are continuously tunable from ~ 1200 to ~ 2400 nm. Using harmonic, sum, and difference frequency-generating crystals outside the OPG, wavelengths from ~ 200 to ~ 10 μm can be generated with average pulse energies varying from 1 to 100 $\mu\text{J}/\text{pulse}$, depending on the wavelength. A prism is used to isolate the desired wavelength from the output of the laser system. Optics currently installed on the beam line allow for component testing at wavelengths from 300 to 2600 nm.

The selected wavelength is spatially filtered and variably attenuated using holographic wire-grid polarizers before reaching the test bench. The laser beam passes through a series of beam splitters before reaching the target. The first beam splitter (BS1) diverts a fraction of the beam to a calibrated photodiode. Each pulse from the detector is captured and measured individually, from which the laser pulse energy can be extracted according to the calibrated energy peak relationship [23]. To reduce the laser pulse-to-pulse energy variation, data corresponding to pulse energies outside one standard deviation from the mean energy are neglected in the analysis. Another beam splitter (BS2) sends light reflected from the target to an infrared (IR) camera for imaging and positioning of the laser spot. A third splitter (BS3) couples a broadband near-IR light source onto the beam axis for illuminating the target. Finally, the laser is focused through the backside of the target using either a $50\times$ or $100\times$ microscope objective mounted to a customized high-precision z-stage used to change the depth at which the laser focuses inside the die.

The laser wavelengths used in this experiment are 1260 and 2200 nm. The laser pulse-to-pulse energy variation is less than 2% and 5%, respectively, for the 1260 and 2200 nm wavelengths. The photon energy and carrier generation mechanisms are listed in Table I for different materials in the device. For a wavelength of 1260 nm, charge will be gen-

TABLE I
MATERIALS PARAMETERS AND CARRIER GENERATION MECHANISM AT TWO DIFFERENT WAVELENGTHS

Material	Band gap	$\lambda=1260$ nm ($E=0.98$ eV)	$\lambda=2200$ nm ($E=0.56$ eV)
$\text{In}_{0.53}\text{Ga}_{0.47}\text{As}$	0.75 eV	SPA/TPA	TPA
$\text{In}_{0.52}\text{Al}_{0.48}\text{As}$	1.46 eV	TPA	NONE
InP	1.35 eV	TPA	NONE

(For materials where both SPA and TPA happen, the dominant mechanism is marked as bold.)

erated in all of the semiconductor materials, either through SPA or TPA. In contrast, for a wavelength of 2200 nm, charge can only be generated in the $\text{In}_{0.53}\text{Ga}_{0.47}\text{As}$ channel and the n^+ InGaAs capping layer. No charge will be generated in the $\text{In}_{0.52}\text{Al}_{0.48}\text{As}$ or InP, since the photon energy is less than half of the material bandgap so that neither SPA nor TPA can take place. As will be shown later, collection of those charges deposited in the InGaAs capping layer is only a small fraction of the total collected charge. Therefore, charge can be generated in a specific layer, allowing the response of that specific layer to be isolated from all the surrounding layers.

Transients are captured using a Teledyne Lecroy LabMaster 10-36Zi-A oscilloscope with 36-GHz front-end bandwidth and 80 GS/s sampling rate. As mentioned above, transients of planar InGaAs quantum-well MOSFETs are also shown as captured by a Tektronix TDS6124C oscilloscope with 12-GHz front-end bandwidth and 20 GS/s sampling rate for comparison. A semiconductor parameter analyzer, HP 4156B, supplied the dc biases through Picosecond Model 5542 bias tees with 50-GHz bandwidth. More details about the electrical measurement setup can be found in [5].

IV. RESULTS AND DISCUSSION

A. System Validation

Charge collection mechanisms in planar InGaAs quantum-well MOSFET have been discussed in [5]. Fig. 3(a) and (b)

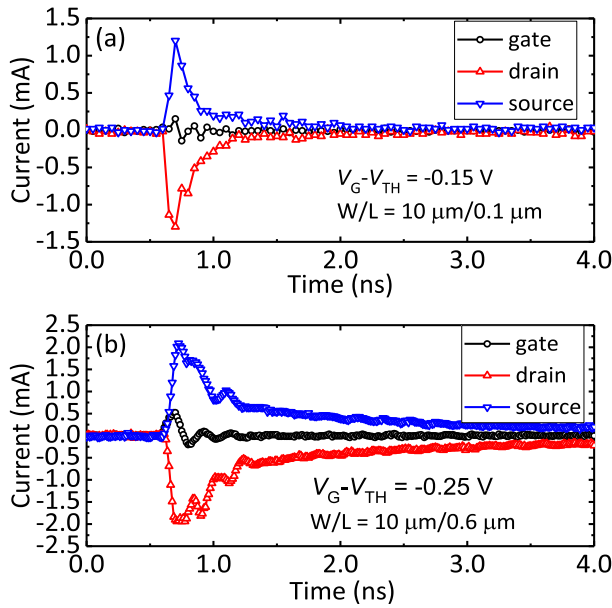


Fig. 3. Typical transients in planar InGaAs quantum-well MOSFET captured by (a) Tektronix TDS6124C oscilloscope and (b) Teledyne Lecroy LabMaster 10-36Zi-A oscilloscope. The strike point is at the center of the device, on top of the gate. The laser wavelength used is 1260 nm. Peak currents differ as a result of different laser energies. $V_D = 0.5$ V.

shows the transients captured by the TDS6124C and LabMaster 10-36Zi-A oscilloscopes, respectively. Transients were generated by a 1260-nm laser.

The rise time of the transients is very short, on the order of 100 ps. As a result, only a single data point is recorded on the rising edge for the TDS6124C oscilloscope, which has 50-ps resolution. It is hard to predict the rising edge shape based on such limited data. However, for the LabMaster 10-36Zi-A oscilloscope, the time resolution is 12.5 ps, which is short enough to resolve the rising edge. By fitting the rising edge with an exponential curve, the rise time constant is estimated to be around 39 ps. This illustrates both the benefit and the need to use a higher bandwidth system to characterize fast signals with more accuracy and precision.

Another feature of the transients shown in Fig. 3(b) is the oscillation signal appearing in the transients. The oscillation period is 0.2 ns. There are many possible reasons for this oscillation, including impedance mismatch and extrinsic RLC oscillation associated with bond wires [24]. Since the bond wire used for this device is relatively long, a few millimeters, here the oscillation is likely related to circuit RLC parameters [24].

Charge collection in InGaAs FinFET devices with $L_G = 50$ nm is compared at two different wavelengths 1260 and 2200 nm, in Fig. 4(a) and (b). Two typical transients are shown, for a device biased in the ON state. The difference in the transient magnitude is due to the laser energy difference at the two wavelengths. The rising edge is well resolved and the relevant time constant is about 40 ps, similar to the planar device. The oscillation is still present in the gate transients, with a period of 0.15 ns. This is likely the result of the shorter bond wires used in the FinFET, compared with the planar

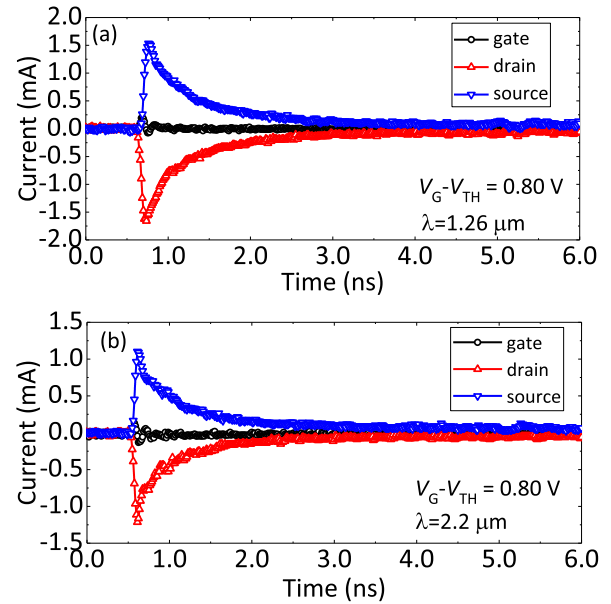


Fig. 4. Typical transients in InGaAs FinFET captured by Teledyne Lecroy LabMaster 10-36Zi-A oscilloscope at (a) $\lambda = 1260$ nm and (b) $\lambda = 2200$ nm at $V_G - V_{TH} = 0.8$ V, $V_D = 0.5$ V. The laser strike is on the drain side, $2 \mu\text{m}$ away from the gate center. $L_G = 50$ nm, $W_{FIN} = 20$ nm.

device.

B. Charge Collection in InGaAs FinFETs

The transient shapes at the two wavelengths are very similar, indicating that the channel layer is critical to the charge collection process. The transient fall times are faster at a wavelength of 2200 nm than at 1260 nm. The time constants obtained by fitting the transients with double exponential decays at 2200 nm, 0.087 ns, and 0.70 ns, are notably smaller than those at 1260 nm, 0.24 ns, and 1.09 ns. This is probably because at 2200 nm, charges are only generated in the channel where they are quickly collected.

Fig. 5(a) and (b) shows the drain current transients for a laser strike on the drain side, $2 \mu\text{m}$ away from the gate center at different gate biases and drain biases, respectively, for a InGaAs FinFET with $L_G = 50$ nm and $W_{FIN} = 20$ nm. The transient peak does not vary with the gate bias, in contrast to the planar III-V MOSFETs [5], [6]. This is because the device is controlled by the two side gates, which have little effect on the substrate below the fin. The tail current increases 50% (evaluated at 2 ns) with increasing gate bias, which is consistent with the response of planar III-V MOSFETs [6]. The drain current is significantly dependent on the applied drain bias. The peak drain current increases approximately $5\times$ when V_D changes from 0.1 to 0.5 V. This is consistent with the increase of the channel electric field with increasing drain bias.

Fig. 6(a) shows the source and drain current transients at different laser strike points along a line scan. The differences in the shapes of the transients, as well as in the peak positions, are a consequence of differences in the details of the charge-collection processes that occur as a function of the excitation location. The source transients are approximately

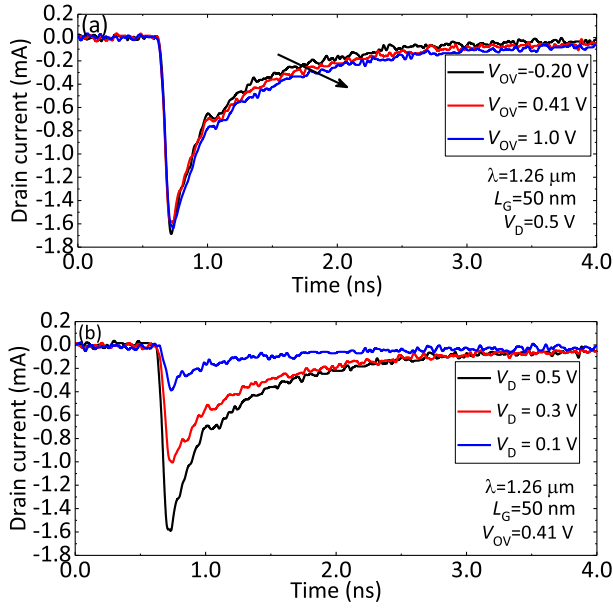


Fig. 5. Drain current transients at different. (a) Gate bias. (b) Drain bias. The laser strike is on the drain side, $2 \mu\text{m}$ from the gate center. $W_{\text{FIN}} = 20 \text{ nm}$. V_{OV} is the overdrive voltage, defined as $V_{\text{GS}} - V_{\text{TH}}$. Laser pulse energy is $0.65 \pm 0.01 \text{ nJ}$.

the inverse of the drain transients (similar magnitude and opposite polarity), no matter whether the strike point is on the source or drain side. This suggests that the transient is mainly associated with source-drain current through the channel. This is consistent with the laser-shunt and parasitic bipolar mechanisms discussed below. The peak drain current amplitude decreases more rapidly on the source side than the drain side, due to the higher electric field on the drain region than the source region. This is also observed in the planar III-V MOSFETs [5], [6].

The comparison between the channel current and junction current can also be seen in Fig. 6(b), which shows the peak drain current along a line scan at different gate biases. Two groups of curves are shown, corresponding to two bias conditions $V_S = 0 \text{ V}$ and $V_S = V_D$. The case with equal source and drain bias represents junction collection only, since there is no electric field along the channel, while the grounded source represents the situation where the source-drain channel current makes a significant contribution. The drain current is almost zero on the source side with $V_S = V_D$. This is because the source collects most of the charge at the source side. With the junction collection, the peak drain current is very small, less than 0.3 mA . However, the channel current is much higher, suggesting that the channel current contributes the most significant charge. This suggests that there is little contribution from the junction collection, which is different from traditional bulk Si devices, and similar to SOI devices [25], and is consistent other III-V devices [30].

The mechanisms of channel current are also investigated. At the center of the gate, the peak drain current is maximum. This is similar to the ion-shunt mechanism observed in Si devices [26], [27]. When an ion track size is comparable to the device gate length, the high density of electron-hole pairs will short the source and drain, contributing to a large prompt

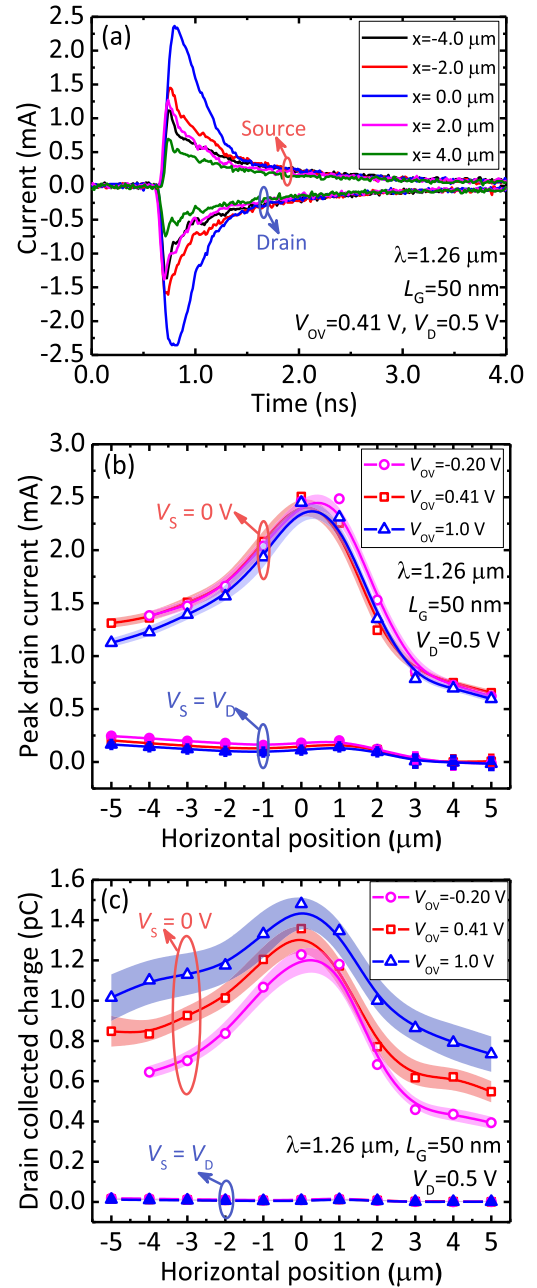


Fig. 6. (a) Source and drain current transients at different laser strike positions along a line scan. (b) and (c) Peak drain current and drain collected charge, respectively, along a line scan at different gate biases. Here the center of the gate is taken as $x = 0 \mu\text{m}$. The negative x coordinate represents the drain side and the positive x coordinate represents the source side. The laser wavelength $\lambda = 1260 \text{ nm}$. The shadow in (b) and (c) represents the standard deviation among the 50 transients recorded at each position. $W_{\text{FIN}} = 20 \text{ nm}$. Laser pulse energy is $0.65 \pm 0.01 \text{ nJ}$.

current. Similarly, in our laser system, the laser spot size is approximately $1.2 \mu\text{m}$, much larger than the gate length. Therefore, it should be expected that the peak drain current is maximum around the gate center. The shunt mechanism alone, however, cannot explain the channel current when the laser strikes away from the gate, for example, $x = \pm 5 \mu\text{m}$. This increase is due to parasitic bipolar effects [4]–[6], which become active when radiation-induced holes accumulate beneath the gate, perturbing the local electrostatic potential, lowering the source to channel barrier, and inducing a source-

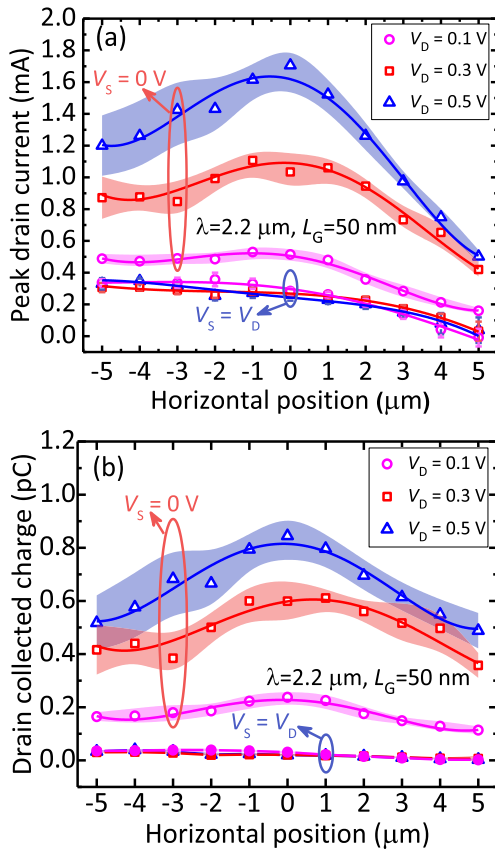


Fig. 7. (a) and (b) Peak drain current and drain collected charge, respectively, along a line scan at different drain biases. The negative x coordinate represents the drain side and the positive x coordinate represents the source side. The laser wavelength $\lambda = 2200$ nm. The shadow represents the standard deviation among the 50 transients recorded at each position. $V_G - V_{TH} = 0.5$ V. $W_{FIN} = 20$ nm.

to-drain current pathway. This will be further illustrated below by technology computer-aided design (TCAD) simulations.

The collected charge along a line scan is shown in Fig. 6(c). The charge is obtained by integrating the captured transients within a time window of 30 ns. The collected charge increases with the gate bias when the source is grounded. This is because the tail current increases with gate bias, as shown in Fig. 5(a). When integrated, the tail current contributes a significant amount of charge. In comparison, the junction-collected charge is much smaller, around 10 fC. However, there is no clear evidence that the deposited charge correlates with the junction collected charge, when the deposited charges are distributed in the channel, buffer, and substrate, as shown in Table I. Therefore, no quantitative conclusions can be drawn. However, for the laser wavelength $\lambda = 2200$ nm, charge is generated only in the channel layer, similar to SOI technology. It has been shown in Si SOI technology that the deposited charge can be empirically estimated from the source/drain transients with the source and drain at the same bias [28]. In our case, this methodology is also applicable at $\lambda = 2200$ nm.

Fig. 7(a) and (b) shows the peak drain current and drain collected charge, similar to Fig. 6(b) and (c), at different drain biases for $\lambda = 2200$ nm. Both the peak drain current and the drain-collected charge increase with the drain bias,

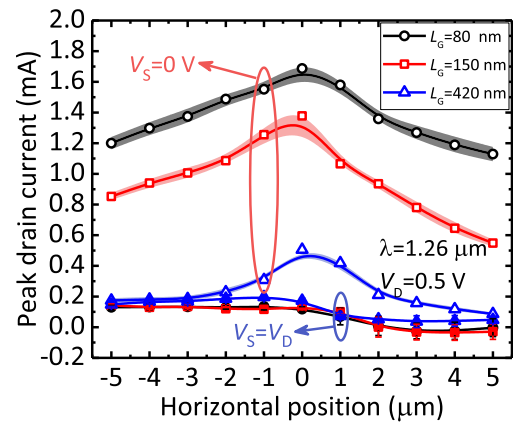


Fig. 8. Peak drain current along a line scan for different gate lengths. The laser wavelength $\lambda = 1260$ nm. The shadow represents the standard deviation among the 50 transients recorded at each position. $V_G - V_{TH} = 0$ V. $W_{FIN} = 30$ nm. Laser pulse energy is 0.65 ± 0.01 nJ.

as illustrated also in Fig. 5(b). The current gain is approximately 6 for $V_D = 0.5$ V at $x = 0$ μm . In addition, the deposited charge is twice the drain collected charge at equal source and drain bias, about 60 fC at $x = 0$ μm . This corresponds to charge enhancement factors of 14, 10, and 4 for $V_D = 0.5, 0.3,$ and 0.1 V, respectively. Similar charge enhancement factors have also been reported in other types of III-V FETs [6], [29], [30]. These large enhancement factors also imply that the junction collection, including collection of those charges deposited in the InGaAs capping layer, plays a minor role in charge collection for this type of device. These results demonstrate the advantage of a tunable wavelength laser system, which allows quantitative analysis of these important device responses.

Parasitic bipolar effects are also observed in the excess OFF-state leakage current in InGaAs quantum-well MOSFETs; the gain is typically inversely proportional to the gate length [31]. Fig. 8 shows the peak drain current along a line scan for different gate lengths for fin width $W_{FIN} = 30$ nm. Two groups of curves are shown, one with source grounded and the other with equal source and drain voltages. The peak drain current decreases with gate length, as expected. For $L_G = 420$ nm, the peak drain currents are approximately equal in the drain side for the two bias conditions, suggesting that the parasitic bipolar action is fully suppressed in the longer channel device. In addition, the sensitive area broadens with decreasing gate length. These results imply that sensitivity to transient radiation effects may increase in these types of devices with technology scaling, which is important to understand for space applications.

The peak drain current dependence on laser energy is investigated in Fig. 9. The peak drain current increases with the laser pulse energy, with a relationship of approximately $I_{DP} \propto E^{0.5}$, where E is the laser pulse energy and I_{DP} is the peak drain current. This sublinear dependence may be related to the complex charge injection profile at $\lambda = 1260$ nm on the one hand, but may also be related with the parasitic bipolar effect which induces the channel current. Further experiments

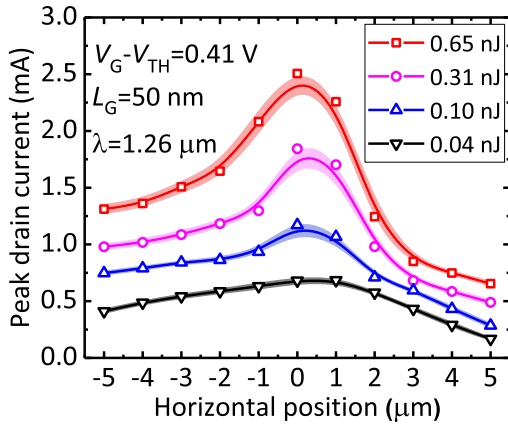


Fig. 9. Peak drain current along a line scan for different laser pulse energies. The shadow represents the standard deviation among the 50 transients recorded at each position. $W_{\text{FIN}} = 20$ nm.

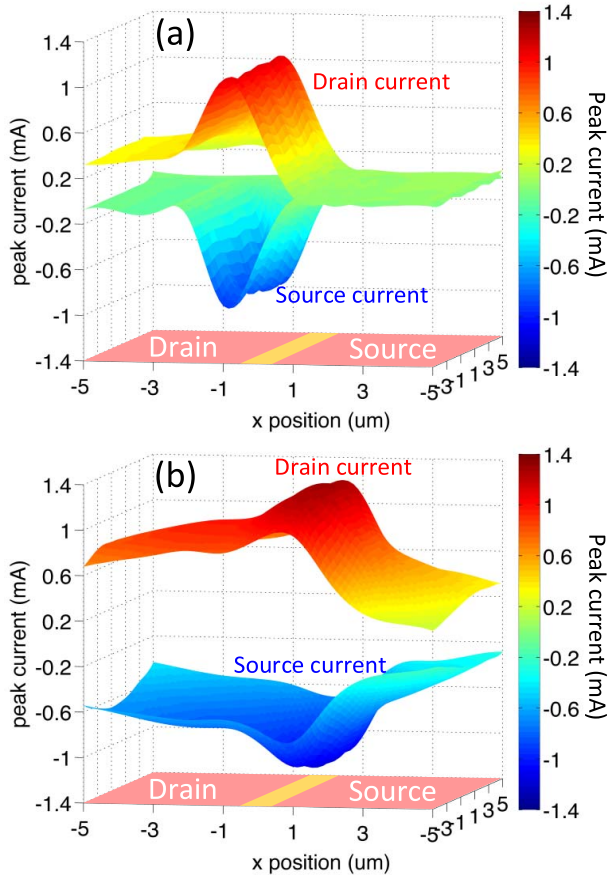


Fig. 10. Peak source and drain current area map for (a) $L_G = 600$ nm and (b) $L_G = 50$ nm. The source current is the top and the drain current is at the bottom. For the area scan, the origin is chosen to be the center of the gate. $W_{\text{FIN}} = 20$ nm.

are needed, for example laser energy dependence tested at $\lambda = 2220$ nm, to elucidate the dependence.

An area mapping of the sensitive region is also performed. The results are shown in Fig. 10(a) and (b) for $L_G = 600$ nm and $L_G = 50$ nm, respectively. There is amplification only around the gate region for $L_G = 600$ nm, consistent with Fig. 8. In the drain region, only the drain junction collects

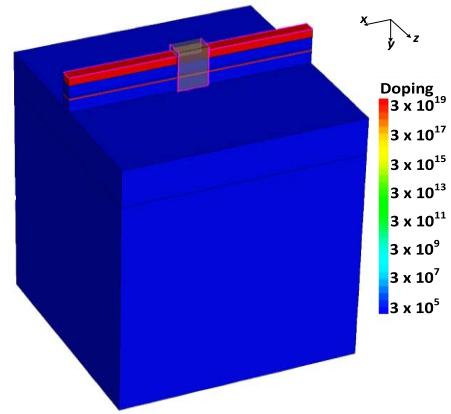


Fig. 11. 3-D TCAD model of InGaAs double-gate FinFET device. $L_G = 50$ nm, $W_{\text{FIN}} = 20$ nm.

charge; while in the source region, the charge collection is greatly suppressed. However, for $L_G = 50$ nm, the sensitive region is much larger, extending deep into the source and drain region, due to larger bipolar gain enhancement, as shown in Fig. 8.

V. TCAD SIMULATIONS

To gain more understanding of the charge collection processes described above, 3-D TCAD simulations are performed with Sentaurus TCAD tools. Fig. 11 shows the TCAD model of the device. The simulated device has a gate length of 50 nm. The thickness of different layers is the same as the measured devices, except that the substrate layer is truncated to 20 μm for ease of simulation. For the simulation, charges corresponding to the amount produced by an oxygen ion strike are introduced into the device at different locations. The injected charge has a Gaussian distribution in both space and time. The center of the strike is 1 ns and the characteristic length of the Gaussian distribution is 50 nm. The amount of deposited charge is 76 fC/ μm for 8 μm . Although the charge distribution used in the simulations is different from the laser irradiation, these results provide a qualitative understanding of the charge collection process.

To illustrate the parasitic bipolar effect, Fig. 12(a) shows the hole density inside the fin at different times for charge injection at $z = 0.63$ μm , on the drain side. Following the charge injection at 1 ns, a large number of electrons and holes are collected in the InGaAs channel within 100 ps, due to the type I heterostructure quantum-well. The hole density remains high for a long time and does not recover to the steady state value even at 30 ns. The accumulated holes close to the source and channel reduce the barrier between source and channel, which can cause additional electrons to be injected from the source and collected by the drain [5], [6], [29], [30].

This is further illustrated in Fig. 12(b), which shows the conduction-band time-evolution along a horizontal cut line, XX', as defined in Fig. 1(a), from the source to drain. The barrier between the source and channel is as high as 0.6 eV before charge injection. However, 200 ps after the strike, the barrier is temporarily removed so that electrons can flow from source to drain. This causes the channel current observed in the experiment. The barrier only partially recovers to 0.1 eV

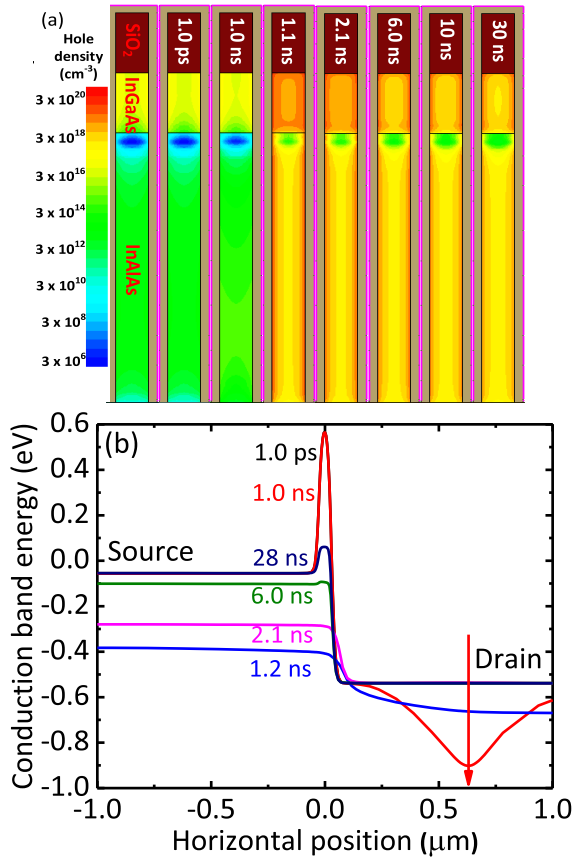


Fig. 12. (a) Hole density inside the fin structure at different times. Shown is a cut plane of the device at $z = 0 \mu\text{m}$, the center of the gate. There are three layers in the fin structure, the top SiO_2 , the middle InGaAs channel and the bottom InAlAs buffer. (b) Conduction band along a horizontal cut line, XX' shown in Fig. 1(a), from source to drain. $V_G = -0.6 \text{ V}$, $V_D = 0.5 \text{ V}$, $V_S = 0 \text{ V}$. The red arrow indicates the location of charge injection. Note that the energy band under the gate at 1 ns is the same as that in pre-strike, at 1 ps.

after 28 ns, implying that the perturbation can last for a long time, probably due to the highly confined FinFET structure. This long lasting transient can increase the sensitivity to radiation.

To understand the role of different layers in the charge collection process, Fig. 13(b) shows the simulated drain current transients for charge injection in different regions, as schematically shown in Fig. 13(a). The current is maximum for the “full” case (defined in Fig. 13), where the charge is injected from the top surface of the device and extends $8 \mu\text{m}$. This result is as expected since the charge injection for the other cases is only a segment of the “full” condition. For charge injection above the channel layer, the current increases promptly but also decays quickly. Thus, the charge deposited above the channel layer is promptly collected.

For the charge injection starting from the buffer layer, the transient peak is delayed 0.3 ns compared with the “channel” case. This delay is caused by the time required for the generated electrons and holes to move to the channel. The current almost overlaps with the “full” case after 2 ns, suggesting that the slow portion comes from the deposited charge below the channel layer. This is different from the diffusion process observed in Si devices [25], since the current

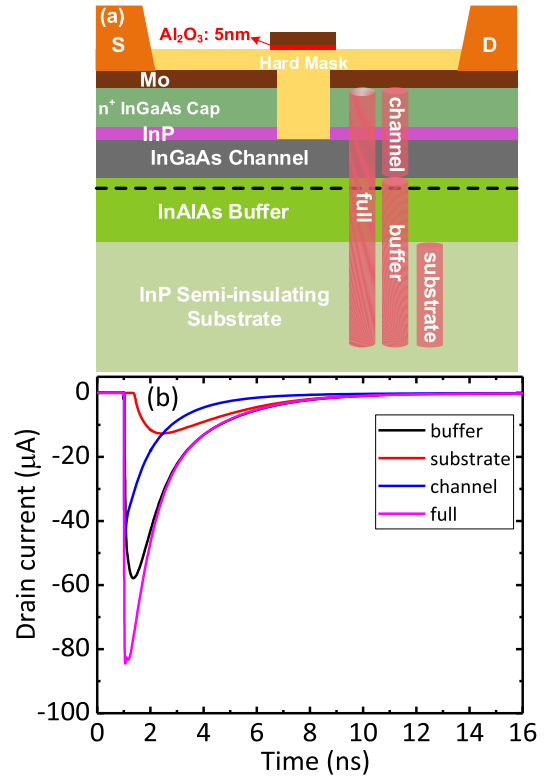


Fig. 13. (a) Different charge injection volumes in the simulation. (b) Drain current transients as a function of time for these areas. Here “full” represents charge injection from the top surface of the device and extends $8 \mu\text{m}$, “channel” represents charge injection from the top of the device up to the channel layer, “buffer” represents charge injection starting from the buffer layer and extending $7.9 \mu\text{m}$, and “substrate” represents charge injection starting from the substrate. The charge injection profiles in the other three conditions are just segments of the “full” condition. Here different charge injection cases are displaced from each other for clear demonstration. In the simulation they overlap; that is, the charge is injected at the same point when projected into the horizontal plane.

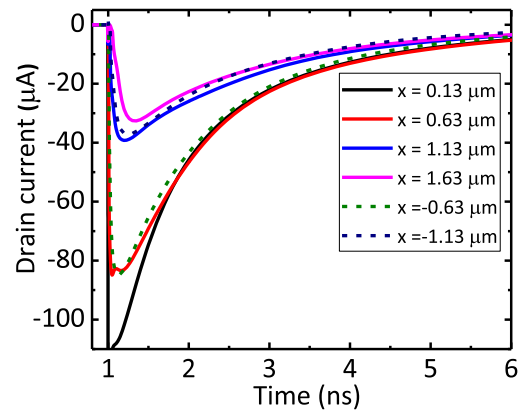


Fig. 14. Drain current transients as a function of time for different strike locations. Here $x = 0$ is at the center of the gate, the positive z coordinate is at the drain side, and the negative x coordinate is at the source side. The solid curves represent strikes in the drain side while the dashed curves represent strikes in the source side.

comes from the channel current caused by parasitic bipolar effects. The current for the “full” case is approximately equal to the sum of the “channel” and “buffer” cases. For the charge injection in the substrate, the transient rises slowly and the

peak is delayed 1 ns compared with the “buffer” case because of the larger distance for carriers to diffuse into the channel layer. After 6 ns, the current overlaps with the “full” case, indicating that the charge deposited in the substrate mainly contributes to the tail currents. After 10 ns, the current is small, but the source-to-channel barrier does not fully recover, as shown in Fig. 12(b). The device operates in the subthreshold region and slowly recovers.

Drain current transients due to strikes at different locations from source to drain are shown in Fig. 14. The position dependence is similar to Fig. 6(a); the current decreases as the strike location moves away from the center of the gate.

VI. SUMMARY AND CONCLUSION

A tunable wavelength laser system and high-resolution transient capture system are introduced for high-mobility MOSFETs. The system has high time resolution, and transient features such as fast edges and oscillations are well resolved. The tunable wavelength laser provides a method to generate charge only in a specific layer of interest, usually the channel layer, since the lowest bandgap typically occurs in the channel of high-mobility MOSFETs. This enables the response of the channel layer to be distinguished from that of the surrounding layers, providing a valuable tool to understand charge collection mechanisms in advanced devices.

The transient current in InGaAs double-gate FinFET devices mostly comes from the channel current, instead of junction collection. The channel current is attributed to the shunt effect around the gate and parasitic bipolar effects. Charge amplification factors as high as 14 are found. The tunable wavelength laser system allows empirically quantitative analysis of the results. In addition, parasitic bipolar effects are shown to be inversely proportional to the device gate length, making scaled devices highly sensitive to radiation.

From TCAD simulations, it is found that the parasitic bipolar effect in these devices is due primarily to radiation-generated holes accumulating in the source and channel, which reduce the source to channel barrier and cause additional electrons to be injected from the source and collected by the drain. Further simulations also show that the charge deposited in the channel layer contributes to the prompt current, while the charge deposited in the buffer layer contributes to a delayed and longer-lasting current. The channel layer is critical in determining the charge collection. Therefore, considering both the geometrical footprint and the charge amplification, the two factors compete with each other in determining the sensitivity of InGaAs FinFETs to single-event effects. Hence, this paper presents important and early insights into charge collection mechanisms in InGaAs FinFETs. Further circuit level analysis will be needed to determine the ultimate sensitivity of this technology, for eventual space application.

REFERENCES

- [1] J. A. del Alamo, “Nanometre-scale electronics with III–V compound semiconductors,” *Nature*, vol. 479, no. 7373, pp. 317–323, Nov. 2011.
- [2] M. Radosavljevic *et al.*, “Electrostatics improvement in 3-D tri-gate over ultra-thin body planar InGaAs quantum well field effect transistors with high-K gate dielectric and scaled gate-to-drain/gate-to-source separation,” in *IEDM Tech. Dig.*, Dec. 2011, pp. 765–768.
- [3] J. J. Gu, Y. Q. Liu, Y. Q. Wu, R. Colby, R. G. Gordon, and P. D. Ye, “First experimental demonstration of gate-all-around III–V MOSFETs by top-down approach,” in *IEDM Tech. Dig.*, Dec. 2011, pp. 769–772.
- [4] D. McMorrow *et al.*, “Single-event phenomena in GaAs devices and circuits,” *IEEE Trans. Nucl. Sci.*, vol. 43, no. 2, pp. 628–644, Apr. 1996.
- [5] K. Ni *et al.*, “Single-event transient response of InGaAs MOSFETs,” *IEEE Trans. Nucl. Sci.*, vol. 61, no. 6, pp. 3550–3556, Dec. 2014.
- [6] K. Ni *et al.*, “Charge collection mechanisms in GaAs MOSFETs,” *IEEE Trans. Nucl. Sci.*, vol. 62, no. 6, pp. 2752–2759, Dec. 2015.
- [7] N. Seifert *et al.*, “Soft error susceptibilities of 22 nm tri-gate devices,” *IEEE Trans. Nucl. Sci.*, vol. 59, no. 6, pp. 2666–2673, Dec. 2012.
- [8] N. Seifert *et al.*, “Soft error rate improvements in 14-nm technology featuring second-generation 3D tri-gate transistors,” *IEEE Trans. Nucl. Sci.*, vol. 62, no. 6, pp. 2570–2577, Dec. 2015.
- [9] Y.-P. Fang and A. S. Oates, “Neutron-induced charge collection simulation of bulk FinFET SRAMs compared with conventional planar SRAMs,” *IEEE Trans. Device Mater. Rel.*, vol. 11, no. 4, pp. 551–554, Dec. 2011.
- [10] J. S. Melinger *et al.*, “Critical evaluation of the pulsed laser method for single event effects testing and fundamental studies,” *IEEE Trans. Nucl. Sci.*, vol. 41, no. 6, pp. 2574–2584, Dec. 1994.
- [11] S. P. Buchner, F. Miller, V. Pouget, and D. P. McMorrow, “Pulsed-laser testing for single-event effects investigations,” *IEEE Trans. Nucl. Sci.*, vol. 60, no. 3, pp. 1852–1875, Jun. 2013.
- [12] D. McMorrow, W. T. Lotshaw, J. S. Melinger, S. Buchner, and R. L. Pease, “Subbandgap laser-induced single event effects: Carrier generation via two-photon absorption,” *IEEE Trans. Nucl. Sci.*, vol. 49, no. 6, pp. 3002–3008, Dec. 2002.
- [13] J. S. Melinger *et al.*, “Pulsed laser-induced single event upset and charge collection measurements as a function of optical penetration depth,” *J. Appl. Phys.*, vol. 84, no. 2, pp. 690–703, Jul. 1998.
- [14] D. McMorrow, S. Buchner, W. T. Lotshaw, J. S. Melinger, M. Maher, and M. W. Savage, “Demonstration of single-event effects induced by through-wafer two-photon absorption,” *IEEE Trans. Nucl. Sci.*, vol. 51, no. 6, pp. 3553–3557, Dec. 2004.
- [15] K. J. Kuhn, “Considerations for ultimate CMOS scaling,” *IEEE Trans. Electron Devices*, vol. 59, no. 7, pp. 1813–1828, Jul. 2012.
- [16] E. X. Zhang *et al.*, “Heavy-ion and laser induced charge collection in SiGe channel pMOSFETs,” *IEEE Trans. Nucl. Sci.*, vol. 61, no. 6, pp. 3187–3192, Dec. 2014.
- [17] I. K. Samsel *et al.*, “Charge collection mechanisms of Ge-channel bulk pMOSFETs,” *IEEE Trans. Nucl. Sci.*, vol. 62, no. 6, pp. 2725–2731, Dec. 2015.
- [18] D. McMorrow *et al.*, “Transient response of semiconductor electronics to ionizing radiation. Recent developments in charge-collection measurement,” *IEEE Trans. Nucl. Sci.*, vol. 54, no. 4, pp. 1010–1017, Aug. 2007.
- [19] R. S. Wagner, N. Bordes, J. M. Bradley, C. J. Maggiore, A. R. Knudson, and A. B. Campbell, “Alpha-, boron-, silicon- and iron-ion-induced current transients in low-capacitance silicon and GaAs diodes,” *IEEE Trans. Nucl. Sci.*, vol. 35, no. 6, pp. 1578–1584, Dec. 1988.
- [20] D. McMorrow *et al.*, “Novel energy-dependent effects revealed in GeV heavy-ion-induced transient measurements of antimony-based III–V HEMTs,” *IEEE Trans. Nucl. Sci.*, vol. 57, no. 6, pp. 3358–3365, Dec. 2010.
- [21] A. Vardi, X. Zhao, and J. A. del Alamo, “Quantum-size effects in sub 10-nm fin width InGaAs FinFETs,” in *IEDM Tech. Dig.*, Dec. 2015, pp. 31.3.1–31.3.4.
- [22] J. Lin, Z. Xin, Y. Tao, D. A. Antoniadis, and J. A. del Alamo, “A new self-aligned quantum-well MOSFET architecture fabricated by a scalable tight-pitch process,” in *IEDM Tech. Dig.*, Dec. 2013, pp. 421–424.
- [23] N. C. Hooten, “Charge collection mechanisms in silicon devices during high-level carrier generation events,” Ph.D. dissertation, Vanderbilt Univ., Nashville, TN, USA, 2014.
- [24] D. McMorrow, A. R. Knudson, and A. B. Campbell, “Fast charge collection in GaAs MESFETs,” *IEEE Trans. Nucl. Sci.*, vol. 37, no. 6, pp. 1902–1908, Dec. 1990.
- [25] R. C. Baumann, “Radiation-induced soft errors in advanced semiconductor technologies,” *IEEE Trans. Device Mater. Rel.*, vol. 5, no. 3, pp. 305–316, Sep. 2005.
- [26] J. R. Hauser, S. E. Diehl-Nagle, A. R. Knudson, A. B. Campbell, W. J. Stapor, and P. Shapiro, “Ion track shunt effects in multi-junction structures,” *IEEE Trans. Nucl. Sci.*, vol. 32, no. 6, pp. 4115–4121, Dec. 1985.
- [27] F. El-Mamouni *et al.*, “Heavy-ion-induced current transients in bulk and SOI FinFETs,” *IEEE Trans. Nucl. Sci.*, vol. 59, no. 6, pp. 2674–2681, Dec. 2012.

- [28] V. Ferlet-Cavrois *et al.*, "Analysis of the transient response of high performance 50-nm partially depleted SOI transistors using a laser probing technique," *IEEE Trans. Nucl. Sci.*, vol. 53, no. 4, pp. 1825–1833, Aug. 2006.
- [29] D. McMorrow *et al.*, "Transient response of III–V field-effect transistors to heavy-ion irradiation," *IEEE Trans. Nucl. Sci.*, vol. 51, no. 6, pp. 3324–3331, Dec. 2004.
- [30] D. McMorrow *et al.*, "Charge-collection mechanisms of heterostructure FETs," *IEEE Trans. Nucl. Sci.*, vol. 41, no. 6, pp. 2055–2062, Dec. 1994.
- [31] J. Lin, D. A. Antoniadis, and J. A. del Alamo, "Physics and mitigation of excess OFF-state current in InGaAs quantum-well MOSFETs," *IEEE Trans. Electron Devices*, vol. 62, no. 5, pp. 1448–1455, May 2015.